ÉCOLE POLYTECHNIQUE FÉDÉRALE DE LAUSANNE

MATHICSE

Mathematics Institute of Computational Science and Engineering

School of Basic Sciences - Section of Mathematics

MATHICSE Technical Report

Nr. 28.2013

September 2013

Thermodynamically consistent orthotropic activation model capturing ventricular systolic wall thickening in cardiac electromechanics

S. Rossi, T. Lassila, R. Ruiz-Baier, A. Sequeira, A. Quarteroni

http://mathicse.epfl.ch

Phone: +41 21 69 37648

Address:
EPFL - SB - MATHICSE (Bâtiment MA)
Station 8 - CH-1015 - Lausanne - Switzerland

Fax: +41 21 69 32545

Thermodynamically consistent orthotropic activation model capturing ventricular systolic wall thickening in cardiac electromechanics

Simone Rossi[†,*], Toni Lassila[*], Ricardo Ruiz-Baier[*], Adélia Sequeira[†]and Alfio Quarteroni[*,‡]

September 11, 2013

Abstract

The complex phenomena underlying mechanical contraction of cardiac cells and their influence in the dynamics of ventricular contraction are extremely important in understanding the overall function of the heart. In this paper we generalize previous contributions on the active strain formulation and propose a new model for the excitation-contraction coupling process. We derive an evolution equation for the active fiber contraction based on configurational forces, which is thermodynamically consistent. Geometrically, we link microscopic and macroscopic deformations giving rise to an orthotropic contraction mechanism that is able to represent physiologically correct thickening of the ventricular wall. A series of numerical tests highlights the importance of considering orthotropic mechanical activation in the heart and illustrates the main features of the proposed model.

1 Introduction

Cardiac muscle is highly heterogeneous and features an anisotropic and overall nonlinear behavior. A helical arrangement of families of co-aligned cardiomyocytes supported by an extracellular fibrous collagen network defines the local macroscopic structure of the tissue and features a complex passive response of the material. During systole the tissue activates and the cardiomyocytes contract. Mechano-chemical activation is mainly governed by the binding of calcium to troponin C, exposing binding sites for myosin on actin filaments. This triggers sarcomere contraction, which can be also modeled as a process that depends on the local strain and strain rate. Despite numerous emerging studies on cardiac contraction mechanisms ranging from experimental observations to theoretical formalisms and mechanistic explanations, the underlying multiscale and multiphysics phenomena governing the excitation-contraction coupling are still far from being fully understood. One often needs to limit the study to a specific sub-aspect of the entire process, compounding all remaining effects into simplified descriptions.

In this work, we focus on the mathematical description of active strain generation at cellular and organ levels. The upscaling strategy is incorporated in the model following an anisotropic active strain formalism [27, 41], where the force balance determining the motion of the tissue depends on local distortion of the microstructure followed by a macroscopic rearrangement of the material recovering compatibility of the deformation. Mathematically, this corresponds to a decomposition of strains. Dissipative effects taking place during ventricular contraction are introduced assuming that the energy is a function of an auxiliary internal state variable, which represents the level of mechanical tissue activation. Then, from

[*]Modeling and Scientific Computing, MATHICSE, École Polytechnique Fédérale de Lausanne, CH-1015 Lausanne, Switzerland. E-mail: {toni.lassila,alfio.quarteroni,simone.rossi,ricardo.ruiz}@epfl.ch

[†]Departamento de Matemática, Instituto Superior Técnico, Av. Rovisco Pais 1, 1049-001 Lisbon, Portugal. E-mail: adelia.sequeira@math.ist.utl.pt

[‡]MOX - Modellistica e Calcolo Scientifico, Dipartimento di Matematica "F. Brioschi", Politecnico di Milano, via Bonardi 9, 20133 Milano, Italy.

Table 1: Nomenclature employed through the text.

$\boldsymbol{F}$	Deformation gradient tensor	$\boldsymbol{F}_A$	Active part of the deformation gradient tensor
$\boldsymbol{E}$	Green-Lagrange strain tensor	$\boldsymbol{f}_0$	Material fiber vector
$\boldsymbol{s}_0$	Material sheetlet vector	$\boldsymbol{n}_0$	Material sheetlet-normal vector
u	Internal energy	η	Entropy
T	Temperature	r	Heat supply
$\mathbf{q}$	Heat flux vector	$\mathcal{P}$	Generalized power
$\boldsymbol{P}$	First Piola-Kirchhoff stress tensor	$\boldsymbol{S}$	Second Piola-Kirchhoff stress tensor
ρ	Material density	ψ	Free energy per unit volume
H	Active stress internal state variable	$\mathbf{n}$	Chemical species vector
γ_j	Macroscopic shortening in the $j-$th direction	ξ_j	Microscopic shortening in the $j-$th direction
μ	viscosity coefficient	R_{FL}	Cardiomyocyte force-length relationship
θ	Fiber rotation angle	$\boldsymbol{\nu}$	Surface normal direction

classical laws of thermodynamics we derive an evolution equation for the active strain, which also depends on local stretch and ionic concentrations. The same theoretical derivation can also be used to define an evolution law for the active stress tensor in usual active stress formulations. Similar thermodynamically consistent models to the one presented herein have been derived in [43, 44, 45] for smooth and skeletal muscle and in [42] for isolated cardiomyocytes. We present here a phenomenological description of the excitation-contraction coupling, but an extension to more physiologically detailed models [25, 29, 38, 51] is conceptually straightforward. Our interest is more oriented to the development of subcellular activation mechanisms tailored for the study of macroscopic cardiac electromechanics. Many studies have focused on descriptions of the contraction in the "mean fiber direction" considering the contraction of the tissue as transversely isotropic. We propose a simple model that links the microscopic and macroscopic deformations explaining cross-fiber shortening.

The validity of our new interpretation is assessed by simulation of the entire cardiac electromechanical function. The passive response of the material is modeled using the orthotropic Holzapfel-Ogden model [13, 16], including fiber and sheetlet directional anisotropy, whereas the tissue electrophysiology is represented by the monodomain equations endowed with the minimal membrane model for human ventricular electrophysiology of Bueno-Orovio *et al.* from [5]. We choose a staggered algorithm to describe the interaction between the electrophysiology and soft tissue mechanics. This allows us to follow the intrinsic differences in the time scales of both phenomena and is computationally less involved than the so-called monolithic schemes (where all subproblems are solved simultaneously) that are, on the other hand, more stable [9, 14, 32].

For the proposed activation model, the knowledge of the directions of anisotropy is essential. In many cases the fiber reconstruction by DT-MRI is usually too noisy to be used in simulations, as such [26]. For this reason, a rule-based fiber field is constructed instead. Here we follow the example in [52] and build sheetlet and fiber fields using simple geometrical and physiological assumptions.

This paper is organized as follows. Section 2 outlines the theoretical settings of the formulation. Starting from the generalized dissipation inequality for isothermal processes, we introduce the active strain formulation and show how to link microscopic and macroscopic deformations. We use the thermodynamical restrictions to build an evolution law for the active strains and we show how the same theoretical setting could be applied to the more common active stress formulation. A model for the macroscopic electromechanical coupling, along with algorithmic considerations is briefly presented in Section 3. Here we also detail the procedure used to construct the fiber and sheetlet fields. Numerical results are collected in Section 4, where we present four test cases to asses the validity of the proposed model. Special emphasis is placed on demonstrating that with the new orthotropic activation model the contraction pattern of the ventricle exhibits the correct physiological amount of wall thickening, torsion, and longitudinal shortening. Finally, in Section 5, we discuss the implications and limitations of our model.

2 Theoretical setting

2.1 Free energy and dissipation inequality

Denoting with u and η the internal energy and the entropy per unit of mass, respectively, the first and second law of thermodynamics in material coordinates read, respectively [7, 12]

$$\rho\dot{u} = \mathbf{S} : \dot{\mathbf{E}} + \rho r - \nabla \cdot \mathbf{q}, \tag{1}$$

$$\rho\dot{\eta} \geq \rho\frac{r}{T} - \nabla \cdot \left(\frac{\mathbf{q}}{T}\right), \tag{2}$$

where ρ is the density of the material in the reference configuration, $\mathbf{S}$ is a referential symmetric stress work conjugate with the strain rate $\dot{\mathbf{E}}$, r is the heat supply, $\mathbf{q}$ is the heat flux vector and T is the temperature. Gradient and divergence operators are taken with respect to the coordinates $\mathbf{X}$ in the reference configuration. It will be useful to consider the stress power $\mathbf{S} : \dot{\mathbf{E}}$ to be given in the form $\mathbf{P} : \dot{\mathbf{F}}$, where $\mathbf{P}$ is the mixed (two-point) first Piola-Kirchhoff stress tensor, conjugate with the rate of the deformation gradient tensor $\dot{\mathbf{F}}$ (see a summary of used notation in Table 1).

Expanding the divergence operator in (2) and using (1) to eliminate r we obtain

$$\rho\dot{\eta} \geq \frac{1}{T^2}\mathbf{q} \cdot \nabla T + \frac{1}{T}\rho\dot{u} - \frac{1}{T}\mathbf{P} : \dot{\mathbf{F}},$$

which can also be written, after some manipulations, as

$$-\rho(\dot{u} - T\dot{\eta}) + \mathbf{P} : \dot{\mathbf{F}} - \frac{1}{T}\mathbf{q} \cdot \nabla T \geq 0.$$

Introducing the Helmholtz free energy per unit of mass, defined as the negative Legendre transformation of the internal energy density with respect to the entropy density $\psi \equiv u - T\eta$, in the previous relation we arrive to the dissipation inequality

$$-\rho(\dot{\psi} + \eta\dot{T}) + \mathbf{P} : \dot{\mathbf{F}} - \frac{1}{T}\mathbf{q} \cdot \nabla T \geq 0.$$

If we restrict to isothermal processes, in which temperature is constant in time, and assume no heat flux, we find

$$-\rho\dot{\psi} + \mathbf{P} : \dot{\mathbf{F}} \geq 0. \tag{3}$$

Following [44, 45] we can extend (3) to the case of generalized internal power $\mathcal{P}$, which leads to

$$-\rho\dot{\psi} + \mathcal{P} \geq 0. \tag{4}$$

2.1.1 Dislocation approach

Experiments on isolated myocytes [38, 49] show that the relative shortening of the cell during active contraction is not large, say between 5-10%. The contraction, due to sliding of the myofilaments, can be interpreted as a microscopic rearrangement of the sarcomeres. Several authors have used this approach to describe deformations both at cellular and organ level [6, 42, 48]. From the mathematical point of view this rearrangement can be achieved through a multiplicative decomposition of the deformation gradient tensor [19, 24] of the form $\mathbf{F} = \mathbf{F}_E\mathbf{F}_M$, where $\mathbf{F}_M$ and $\mathbf{F}_E$ are the microscopic and elastic deformation gradient tensors, respectively. Such a decomposition accounts for introducing an intermediate frame between the reference and the deformed configurations. The microscopic part of the deformation gradient takes the form [27]

$$\mathbf{F}_M = \mathbf{I} + \xi_f \boldsymbol{f}_0 \otimes \boldsymbol{f}_0 + \xi_s \boldsymbol{s}_0 \otimes \boldsymbol{s}_0 + \xi_n \boldsymbol{n}_0 \otimes \boldsymbol{n}_0,$$

and it is usually assumed that $\det \mathbf{F}_M = J_M = 1$ and $\xi_s = \xi_n$, so that when a cell contracts in its longitudinal direction it expands in the orthogonal directions. If an experimental fiber shortening of about 10% is considered, then this strategy fails to reproduce physiological wall thickening. Present

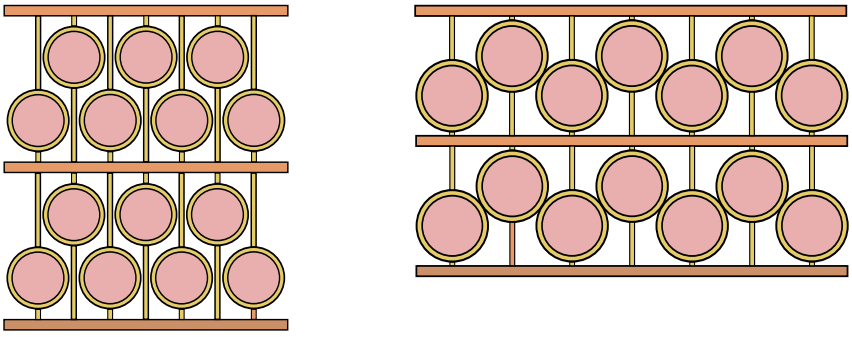

Figure 1: Schematic view of tissue contraction. Cells are surrounded by inextensible collagen filaments attached to horizontal sheets of collagen. The horizontal layers can slide over each other. During contraction, cellular cross section diameter increases and the sheets get closer due to the inextensibility of collagen filaments. Our hypothesis is that wall thickening is due to rearrangement of cardiomyocytes in each layer.

models of cardiac function are not able to explain ventricular wall thickening, being the role of collagen sheetlets at the micro and macro levels still poorly understood [35]. Nevertheless, it is known (see e.g. [20]) that transverse shear along the collagen planes is the main responsible for normal systolic wall thickening, suggesting that different layers of myocytes can "slide" over the collagen. To include the hypothesis of sliding sheetlets, we propose to introduce a macroscopic rearrangement mechanism that occurs simultaneously with a microscopical rearrangement, described as follows

$$\mathbf{F} = \mathbf{F}_E \mathbf{F}_S \mathbf{F}_M. \tag{5}$$

We assume that fiber shortening is not influenced by the sliding process and, therefore, the sliding sheetlet deformation gradient $\mathbf{F}_S$ can be written as

$$\mathbf{F}_S = \mathbf{I} + \zeta_s \boldsymbol{s}_0 \otimes \boldsymbol{s}_0 + \zeta_n \boldsymbol{n}_0 \otimes \boldsymbol{n}_0,$$

which implies that the order of multiplication of the microscopic and macroscopic deformation tensors in (5) is irrelevant since $\mathbf{F}_S \mathbf{F}_M = \mathbf{F}_M \mathbf{F}_S$. Notice that this assumption leads to the definition of a total active deformation gradient tensor in the form

$$\mathbf{F} = \mathbf{F}_E \mathbf{F}_A, \tag{6}$$

with

$$\mathbf{F}_A = \mathbf{I} + \gamma_f \boldsymbol{f}_0 \otimes \boldsymbol{f}_0 + \gamma_s \boldsymbol{s}_0 \otimes \boldsymbol{s}_0 + \gamma_n \boldsymbol{n}_0 \otimes \boldsymbol{n}_0,$$

and $\gamma_i = \zeta_i + \xi_i + \zeta_i \xi_i$ for $i \in \{s, n\}$ and $\gamma_f = \xi_f$.

2.2 Linking micro to macro

While measurement of fiber strains in the left ventricle are in agreement with longitudinal strains measured in isolated cardiomyocytes [33, 51], strain measurements along cross-fiber directions in left ventricular wall indicate that cross-fiber shortening is greater than longitudinal fiber shortening, except for the epicardial region [36, 22]. We explain this macroscopic behavior through a simple geometrical model that links the microscopic deformation with the macroscopic one.

Microscopical cardiomyocyte cross-thickening alone cannot explain the large deformations of the tissue. If a single cell shortens about 6% in its longitudinal direction, it expands about 3% in the others. If during contraction the cells would remain in the same alignment state, the macroscopic thickening would

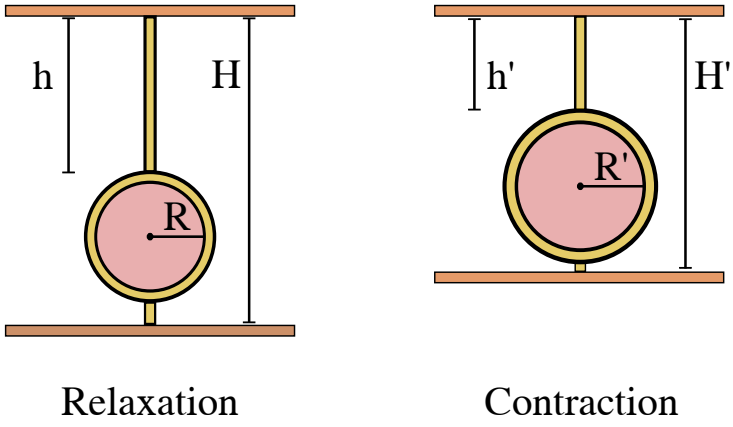

Figure 2: Representation of the cross-fiber shortening model. The inextensible collagen fiber wraps around the cell ω times and then connects with the horizontal layers. When the cell contracts, its radius enlarges and the two collagen sheetlets get closer. The macroscopic wall thickening γ_s is a function of the cross-fiber shortening γ_n and it is found using volume conservation.

be proportional to the microscopic one and to the number of transmural cells. This is in contrast with experience, as the left ventricular wall can thicken up to 40% of its diastolic value [35]. To obtain such a large deformation, different mechanisms must take place. Starting from the idea of sliding collagen sheetlets, we use the fact that cardiomyocytes are interwoven in an inextensible collagen skeleton. We illustrate this idea in Fig. 1. Our hypothesis is that cells in the resting state are surrounded by collagen and ordered in layers which, during contraction, slide one over each other. To create wall thickening we conjecture that, during contraction cells lying in the same horizontal layer tend to line up.

Considering the simple representation depicted in Fig. 2 we derive cross-fiber shortening. We suppose that a single cell is surrounded by an inextensible filament of collagen of length L wrapping around the cells ω times and connecting to the collagen sheetlet. When the cell is in resting state, we denote with R the cell cross-section radius and with h the distance between cell boundary and collagen thick layer, such that the total height of the system H is $2R + h$. In the contracted state, we denote with R' the cross-section radius of the contracted cell, h' the new distance between the cell and the collagen sheetlets such that $H' = 2R' + h'$. By definition the macroscopic shortening in the cross-fiber direction is $\zeta_n = (H' - H)/H$. Using the fact that the contracted cell radius is $R' = R(1 + \xi_n)$, where ξ_n is the microscopic cross-fiber thickening, we find

$$H' - H = 2R\xi_n + h' - h.$$

Simple geometrical arguments show that $L = 2\omega\pi R + h$ and $L' = 2\omega\pi R' + h'$. Enforcing $L' = L$, we can solve for $h' - h$, which leads to

$$H' - H = 2\left(1 - \omega\pi\right) R\xi_n.$$

Eventually, we find that the macroscopic configurational cross-fiber strain is given by

$$\zeta_n = \frac{1 - \omega\pi}{\dfrac{h}{R} + 1}\xi_n = \kappa'\xi_n,$$

with $\kappa' < 0$, and therefore the total cross-fiber strain reads

$$\gamma_n = (1 + \kappa')\xi_n + \kappa'\xi_n^2. \tag{7}$$

Using now microscopical mass conservation, we can write ξ_n as a function of ξ_f, that is $\xi_f = 1/\sqrt{1 + \xi_f} - 1 = -\xi_f/2 + O(\xi_f^2)$. Introducing the linearization in (7), we find the following relation

between the macroscopic cross-fiber shortening and the cellular longitudinal shortening

$$\gamma_n \simeq -\frac{1+\kappa'}{2}\xi_f = \kappa\xi_f.$$

The parameter $\kappa := -(1+\kappa')/2 > 0$ is the link between the microscopic and the macroscopic deformations and its magnitude depends on the transmural and circumferential position (see [2]). In the following we will consider κ as a constant parameter with value 4, according to experimental observations [36]. To conclude, the above considerations yield the following assumptions on the coefficients of the orthotropic activation

$$\gamma_f = \xi_f, \quad \gamma_n = \kappa\xi_f, \quad \gamma_s = \frac{1}{(1+\gamma_f)(1+\gamma_n)} - 1, \tag{8}$$

where the last relation follows from the volume conservation condition $\det \mathbf{F}_A = J_A = 1$.

2.3 Thermodynamical conditions

Decomposition (6) suggests that the active deformation gradient tensor can be regarded as the internal state variable describing mechanical activation. In practice we consider a free energy ψ additively decomposed as

$$\psi(\mathbf{F}_E, \mathbf{n}) = \psi(\mathbf{F}, \mathbf{F}_A, \mathbf{n}) = \psi_P(\mathbf{F}) + \psi_A(\mathbf{F}, \mathbf{F}_A) + \psi_C(\mathbf{n}). \tag{9}$$

Active deformations (here accounted by $\mathbf{F}_A$) are affected by crossbridge dynamics and ionic activity. Active stress is typically considered either as the sum of the densities of crossbridges in strong configuration, or simply as the calcium concentration [17, 29, 50].

Following [44] we suppose that there exists a microscopic stress $\mathbf{P}_A$ yielding the microscopical stress power $\mathbf{P}_A : \dot{\mathbf{F}}_A$. The mixed tensor $\mathbf{P}_A$ is a function of subcellular chemical quantities encoded in $\mathbf{n}$. Therefore the total internal power can be written as

$$\mathcal{P} = \mathbf{P} : \dot{\mathbf{F}} + \mathbf{P}_A : \dot{\mathbf{F}}_A. \tag{10}$$

Introducing (10) in the generalized dissipation inequality (4) we obtain

$$\begin{aligned} &\left(\mathbf{P} - \frac{\partial \psi_P}{\partial \mathbf{F}} - \frac{\partial \psi_A}{\partial \mathbf{F}}\right) : \dot{\mathbf{F}} \\ &\quad + \left(\mathbf{P}_A - \frac{\partial \psi_A}{\partial \mathbf{F}_A}\right) : \dot{\mathbf{F}}_A - \frac{\partial \psi_C}{\partial \mathbf{n}}\dot{\mathbf{n}} = 0. \end{aligned} \tag{11}$$

The quantity $\dfrac{\partial \psi_A}{\partial \mathbf{F}_A}$ represents the *configurational forces* associated with $\mathbf{F}_A$. Relation (11) holds in particular for

$$\mathbf{P} = \frac{\partial \psi_P}{\partial \mathbf{F}} + \frac{\partial \psi_A}{\partial \mathbf{F}}, \tag{12}$$

$$\mu_A \dot{\mathbf{F}}_A = \mathbf{P}_A(\mathbf{n}) - \frac{\partial \psi_A}{\partial \mathbf{F}_A}, \tag{13}$$

$$0 \leq \frac{\partial \psi_C}{\partial \mathbf{n}} \cdot \dot{\mathbf{n}}.$$

2.4 Constitutive assumptions

If cardiac tissue is not activated, its (passive) mechanical response can be accurately reproduced with orthotropic material laws [16]. The different mechanical contraction properties along the preferred directions oriented according to fibers and collagen sheetlets can be incorporated by taking

$$\begin{aligned} \psi(\mathbf{F}, \mathbf{I}, \mathbf{0}) = \frac{a}{2b} e^{b(I_1-3)} + \frac{a_{fs}}{2b_{fs}}\left[e^{b_{fs} I_{8,fs}^2} - 1\right] \\ + \sum_{i \in \{f,s\}} \frac{a_i}{2b_i}\left[e^{b_i (I_{4,i}-1)^2} - 1\right], \end{aligned} \tag{14}$$

as suggested also in [16, 14].

In what follows we assume that $\psi_P = 0$ and we focus on the active part of the energy, resulting from (14) in the expression

$$\begin{aligned}\psi_A(\mathbf{F}_E) = \frac{a}{2b}e^{b(I_1^E-3)} + \frac{a_{fs}}{2b_{fs}}\left[e^{b_{fs}(I_{8,fs}^E)^2}-1\right] \\ + \sum_{i\in\{f,s\}}\frac{a_i}{2b_i}\left[e^{b_i(I_{4,i}^E-1)^2}-1\right],\end{aligned} \tag{15}$$

where the elastic invariants are given by (see also [39])

$$\begin{aligned}I_1^E &= \left[1-\frac{\gamma_n(\gamma_n+2)}{(\gamma_n+1)^2}\right]I_1 + \left[\gamma_n\frac{\gamma_n+2}{(\gamma_n+1)^2} - \gamma_f\frac{\gamma_f+2}{(\gamma_f+1)^2}\right]I_{4,f} \\ &\quad + \left[\gamma_n\frac{\gamma_n+2}{(\gamma_n+1)^2} - \gamma_s\frac{\gamma_s+2}{(\gamma_s+1)^2}\right]I_{4,s}, \\ I_{4,f}^E &= \frac{I_{4,f}}{(\gamma_f+1)^2},\ I_{4,s}^E = \frac{I_{4,s}}{(\gamma_s+1)^2},\ I_{8,fs}^E = \frac{I_{8,fs}}{(\gamma_f+1)(\gamma_s+1)}.\end{aligned}$$

2.5 Active strain dynamics

Regarding (13) as the evolution equation for $\mathbf{F}_A$, one still needs to specify the active stress $\mathbf{P}_A$. The vast majority of experimental studies of active forces focus mainly on the longitudinal fiber direction, making the prescription of the dynamics of all components of the active stress difficult. A projection of the evolution equation on the fiber direction gives

$$\eta_A\dot{\gamma}_f = \left(\mathbf{P}_A - \frac{\partial\psi_C}{\partial\mathbf{F}_A}\right) : \boldsymbol{f}_0\otimes\boldsymbol{f}_0. \tag{16}$$

After some manipulations, the second term on the right hand side of (16) can be written as

$$\frac{\partial\psi_C}{\partial\mathbf{F}_A} : \boldsymbol{f}_0\otimes\boldsymbol{f}_0 = -2\left(\frac{\partial\psi_C}{\partial I_1^E} + \frac{\partial\psi_C}{\partial I_{4,f}^E}\right)\frac{I_{4,f}}{(1+\gamma_f)^3}. \tag{17}$$

The active stress $\mathbf{P}_A$ is directly related to the fraction of crossbridges in the strong configuration, as pointed out in [43, 44, 45]. However, the detailed crossbridge dynamics is rarely available within phenomenological descriptions of the excitation-contraction coupling. Therefore we suppose that active stresses depend on a single quantity n, to be specified later on. Then, it is clear from (17) that even when n vanishes, the tensor $\mathbf{P}_A$ cannot be zero. Let us denote with n_0 the diastolic value of the quantity n and assume that for $n = n_0$, $\dot{\gamma}_f$ is zero. This implies that $\mathbf{P}_A|_{n=n_0} = \partial\psi_C/\partial\mathbf{F}_A$. Moreover the evolution of the active strain strongly depends on the chosen constitutive law. Since both the functional form of the energy and the values of the corresponding parameters determining the material response are still controversial, we "normalize" the active strain dynamics so that it results independent of material parameters. Then the active stress $\mathbf{P}_A$ projected onto the fiber direction is a function of the amount of activation n, the actual stretch of the tissue $I_{4,f}$, and of the prestretch. More precisely, we suppose that

$$\mathbf{P}_A : \boldsymbol{f}_0\otimes\boldsymbol{f}_0 = \left(\frac{\partial\psi_C}{\partial I_1^E} + \frac{\partial\psi_C}{\partial I_{4,f}^E}\right)\left(F_A - \frac{2I_{4,f}}{(1+\gamma_f)^3}\right),$$

where F_A is the part of the active force exerted along the fiber direction which describes its dependence on the subcellular kinetics. To retrieve a material parameter-independent evolution law for the active strain we further assume that $\eta_A = \bar{\eta}_A\left(\partial\psi_C/\partial I_1^E + \partial\psi_C/\partial I_{4,f}^E\right)$, which is always positive (except for materials with negative stiffness, not considered herein).

Derivation of the corresponding energies and parameter normalization give the following dynamics for the active strain

$$\bar{\eta}_A \dot{\gamma}_f = F_A + \frac{2I_{4,f}}{(1+\gamma_f)^3} - \left.\frac{2I_{4,f}}{(1+\gamma_f)^3}\right|_{n=n_0}.$$

Finally, as we expect that $\gamma_f = 0$ for $n = n_0$, we deduce that

$$\bar{\eta}_A \dot{\gamma}_f = F_A + \frac{2I_{4,f}}{(1+\gamma_f)^3} - 2I_{4,f}|_{n=n_0}. \tag{18}$$

The excitation-contraction model is completed assuming that

$$F_A = \alpha f(n) R_{FL}(I_{4,f}),$$

where α represents the active force of a single contractile unit (sarcomere) and $f(n)$ is the activation of the whole tissue. Here $R_{FL}(I_{4,f})$ is the sarcomere force-length relationship of intact cardiac cells, fitted from [47] by the following function (see [42])

$$\begin{aligned} R_{FL}(I_{4,f}) = \chi_{[SL_{\min}, SL_{\max}]} \Bigg\{ & \frac{c_0}{2} \\ & + \sum_{n=1}^{3} [c_n \sin(n I_{4,f} l_0) + d_n \cos(n I_{4,f} l_0)] \Bigg\}, \end{aligned} \tag{19}$$

where l_0 stands for the initial sarcomere length (SL) and $\chi_{[SL_{\min}, SL_{\max}]}$ is the characteristic function of the interval $[SL_{\min}, SL_{\max}]$. Many other representations, as e.g. those analyzed in [3] incorporate active contractile forces depending on the local cell stretch.

Finally, we assume that $f(n) = (n - n_0)^2$ and we observe that the dynamic behavior of the viscosity η_A can be represented proportionally to n, i.e., $\bar{\eta}_A = \widehat{\eta}_A n^2$, where $\bar{\eta}_A$ is a strictly positive constant (see e.g. [45, 46]).

2.6 Active stress formulation

An alternative approach to the one presented above, typically more common in cardiac mechanics, consists in an additive decomposition of the stress tensor. In what follows we show that it is possible to use a consistent thermodynamical framework also for this formulation. We first introduce a new state variable H, linking the microscopic and the macroscopic phenomena. The rate of change of H is generally described by a nonlinear function $\dot{H} = f(\mathbf{F}, H, \mathbf{n})$, where $\mathbf{n}$ represents chemical species driving mechanical activation. In this case we assume the free energy to be a function of deformation $\mathbf{F}$, activation level H and chemical species $\mathbf{n}$,

$$\psi = \psi(\mathbf{F}, H, \mathbf{n}).$$

An active stress model (tacitly) considers active deformations deriving from the following decomposition of the free energy

$$\psi(\mathbf{F}, H) = \psi_P(\mathbf{F}) + \psi_A(\mathbf{F})\psi_B(H) + \psi_C(\mathbf{n}),$$

whereas the internal power is assumed as

$$\mathcal{P} = \mathbf{P} : \dot{\mathbf{F}} + \beta \dot{H}.$$

Applying (4) and the assumptions above we get

$$\begin{aligned} & \left(\mathbf{P} - \frac{\partial \psi_P}{\partial \mathbf{F}} - \psi_B \frac{\partial \psi_A}{\partial \mathbf{F}} \right) : \dot{\mathbf{F}} \\ & + \left(\beta - \psi_A \frac{\partial \psi_B}{\partial H} \right) \dot{H} - \frac{\partial \psi_C}{\partial \mathbf{n}} \cdot \dot{\mathbf{n}} \geq 0. \end{aligned}$$

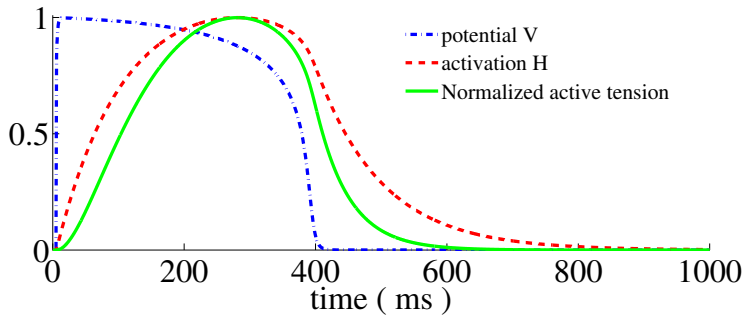

Figure 3: Active stress evolution according to (21) with $\beta(V) = 2.279 T_{\max} V$ kPa and $\mu = 0.001$ kPa.

By assuming that all terms in the previous inequality are non-negative, we have, in particular

$$\mathbf{P} = \frac{\partial \psi_P}{\partial \mathbf{F}} + \psi_B \frac{\partial \psi_A}{\partial \mathbf{F}} \tag{20}$$

$$\mu_H \dot{H} = \beta(\mathbf{n}) - \psi_A \frac{\partial \psi_B}{\partial H} \tag{21}$$

$$0 \leq \frac{\partial \psi_C}{\partial \mathbf{n}} \cdot \dot{\mathbf{n}}.$$

More precisely, (20) is the definition of the total stress, whereas (21) can be regarded as an evolution equation for the mechanical activation.

As an illustrative example, we show how it is possible to derive a simple phenomenological model, similar to the one proposed in [28] and used by several authors [11, 9, 53] (modulus some modifications). In these models the total active tension, denoted with T_a, is described by the equation

$$\dot{T}_a = \epsilon(V)(k_{T_a} V - T_a),$$

where V is the cardiac transmembrane potential.

We now apply the theory developed above to derive the same mechanical assumptions of the original model. To achieve this, we suppose that the total energy is given by

$$\psi(\mathbf{F}, H) = \psi_P(\mathbf{F}) + T_{\max} H^2 J,$$

where $J = \det \mathbf{F}$. Then, using (20) and assuming material incompressibility $J = 1$, the resulting total stress is

$$\mathbf{P} = \mathbf{P}_P + T_{\max} H^2 \mathbf{F}^{-T},$$

and it coincides with that in [28]. The dynamics of the mechanical activation then follows from (21):

$$\mu \dot{H} = \beta(V) - 2 T_{\max} H.$$

Choosing $\beta(V) = \alpha V$ with $\alpha = 2.279\, T_{\max}$ kPa and $\mu = 0.001$ kPa, we obtain the evolution shown in Fig. 3.

We stress that the form of the total energy used in [28] does not satisfy the so-called *unconditionally strong ellipticity condition* (see e.g. [1]). Different evolution laws for the active tension could be obtained by assuming that $\psi_A(\mathbf{F})$ is a function of the fiber elongation $I_{4,f}$. These should follow from the assumptions on the tensorial form of the active stress, as for example in [9, 11].

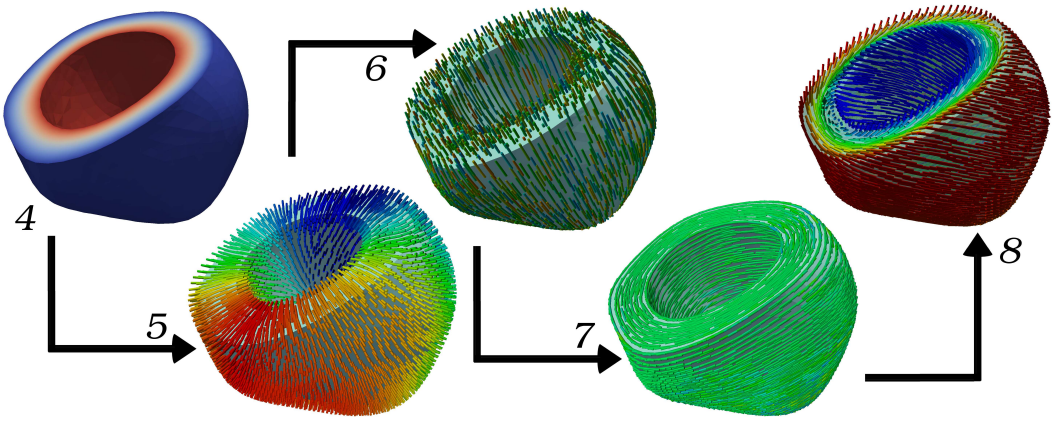

Figure 4: Steps to create the sheetlets and fiber directions. Referring to steps 4 - 8 in Algorithm 1, following the arrows: step 4) solution of problem (23); step 5) sheetlet direction $\boldsymbol{s}_0$; step 6) projection vector $\mathbf{k_p}/\|\mathbf{k_p}\|$; step 7) flat fiber field $\widetilde{\boldsymbol{f}}_0$; step 8) fiber field $\boldsymbol{f}_0$.

3 Coupling with cardiac electrophysiology

3.1 Macroscopic electromechanical coupling

Under physiological conditions, electrical activation of cardiac cells precedes mechanical contraction of the muscle. In addition, calcium dynamics are tightly related to the action of other ionic concentrations and currents through the cellular membrane. To account for the electrophysiological activity in cardiac tissue we incorporate the classical monodomain equations endowed with the model for human epicardial action potential introduced in [5]. The unknowns are the transmembrane potential V and all major ion channels and calcium dynamics are encoded in a vector $\boldsymbol{w}$ of gating variables. The system, written in the reference configuration Ω_0, reads

$$\begin{aligned} C_m\chi_m\partial_t V - \nabla\cdot(\mathbf{F}^{-1}\mathbf{G}\mathbf{F}^{-T}\nabla V) + \chi_m I(V,\boldsymbol{w}) &= I_{\text{stim}}, \\ \mathrm{d}_t\boldsymbol{w} - \boldsymbol{r}(V,\boldsymbol{w}) &= \mathbf{0}, \end{aligned} \tag{22}$$

where $I, \boldsymbol{r}$ are the reaction terms linking macroscopic propagation of potential and cellular dynamics, specified in [5], I_{stim} is an externally applied source, C_m is the specific membrane capacitance per unit area, χ_m is the surface-to-volume ratio of the cardiomyocytes, and $\mathbf{G}$ is a transversely isotropic conductivity tensor representing different myocardial propagation velocities σ_f, σ_s in the directions $\boldsymbol{f}_0$ and $\boldsymbol{s}_0$, respectively. From e.g. (18) it is evident that the electrical activity influences directly the mechanical activation. A basic two-way coupling is achieved by assuming that the electrophysiology is affected by the macroscopic tissue deformation through the geometrical nonlinearity arising from the change of reference ($\mathbf{F}$ appears in the diffusion term of (22)). Other effects, such as stretch activated currents, do not play any major role in the cases studied herein and are therefore neglected.

3.2 Rule-based fiber and sheetlet directions

To test the model on ventricular geometries we need data of fibers and sheetlet directions. While fiber fields taken from MRI are now commonly available, sheetlet orientation data is far more rare and therefore many heart models discard them. Several recent studies on computational cardiac modeling have detailed computational strategies to reconstruct fiber and sheetlet fields based on geometrical rules [15]. We propose here a modified version of the algorithm studied in [52] that allows for an additional reduction in computational cost. The underlying assumption is based on approximating the sheetlet directions to be "radial", curl-free and divergence-free using a Helmholtz decomposition (see e.g. [10]). Let us assume that $\nabla\wedge\boldsymbol{s}_0 = 0$. Then, there exists a scalar potential ϕ such that $\boldsymbol{s}_0 = \nabla\phi$. Therefore, to find the sheetlet

Algorithm 1 – Rule-based sheetlet and fiber directions

1: Set θ_{epi}, θ_{endo}
2: Set the ventricular centerline vector $\mathbf{k}$,
3: Impose BC in (23), e.g. $\phi|_{epi} = 0$, $\phi|_{endo} = 1$,
4: Find ϕ solving problem (23),
5: Compute sheetlet direction as $\boldsymbol{s}_0 = \nabla\phi/\|\nabla\phi\|$,
6: Compute the projection of $\mathbf{k}_p = \mathbf{k} - (\mathbf{k}, \boldsymbol{s}_0)\boldsymbol{s}_0$,
7: Compute the flat fiber field $\widetilde{\mathbf{f}}_0 = \boldsymbol{s}_0 \wedge \mathbf{k}_p/\|\mathbf{k}_p\|$,
8: Rotate the fiber field using (24) and (25).

field, we need to find the potential ϕ, which, taking the divergence of $\boldsymbol{s}_0$, satisfies a Laplace equation supplemented with a set of boundary conditions

$$\begin{aligned} \Delta\phi &= 0 \quad \text{in } \Omega_0, \\ \phi &= g \quad \text{on } \Gamma_D, \\ \frac{\partial\phi}{\partial\nu} &= h \quad \text{on } \Gamma_N. \end{aligned} \tag{23}$$

Typically $h = 0$ on the base, while $g = 0$ on the endocardium, and $g = 1$ on the epicardium. After solving the potential problem with the FEM we use the patch gradient recovery method to find $\boldsymbol{s}_0 = \nabla\phi/||\nabla\phi||$. Let $\mathbf{k}$ be the vector parallel to the ventricular centerline and pointing apex-to-base. Then its projection $\mathbf{k}_p$ on the plane orthogonal to $\boldsymbol{s}_0$ is given by

$$\mathbf{k}_p = \mathbf{k} - (\mathbf{k} \cdot \boldsymbol{s}_0)\, \boldsymbol{s}_0.$$

An initial fiber field (with zero component along the centerline) is defined by $\widetilde{\mathbf{f}}_0 = \boldsymbol{s}_0 \wedge (\mathbf{k}_p/||\mathbf{k}_p||)$. We then create a rotation matrix $\mathbf{R}_{\boldsymbol{s}_0}(\phi)$ which describes the rotation of the fiber field around the $\boldsymbol{s}_0$-axis. Supposing a one-to-one correspondence between the rotation angle and the potential ϕ, we end up with

$$\boldsymbol{f}_0 = \mathbf{R}_{\boldsymbol{s}_0}(\phi)\widetilde{\boldsymbol{f}}_0. \tag{24}$$

Given the rotation angle $\theta = \theta(\phi)$, the rotation matrix $\mathbf{R}_{\boldsymbol{s}_0}(\theta)$ is found through the Rodrigues' rotation formula

$$\mathbf{R}_{\boldsymbol{s}_0}(\theta) = \mathbf{I} + \sin(\theta)\,[\boldsymbol{s}_0]_\times + 2\sin^2(\theta/2)\,[\boldsymbol{s}_0 \otimes \boldsymbol{s}_0 - \mathbf{I}]\,,$$

where $[\boldsymbol{s}_0]_\times$ is the cross-product matrix defined as

$$[\boldsymbol{s}_0]_\times = \begin{pmatrix} 0 & -s_{0,z} & s_{0,y} \\ s_{0,z} & 0 & -s_{0,x} \\ -s_{0,y} & s_{0,x} & 0 \end{pmatrix}.$$

We will suppose the following linear [26] relationship between the potential ϕ and the rotation angle θ

$$\theta = (\theta_{epi} - \theta_{endo})\phi + \theta_{endo}, \tag{25}$$

where θ_{epi} and θ_{endo} are the possible values of the angle rotation on the epicardium and on the endocardium, respectively. The procedure to create the rule-based fiber field is outlined in Algorithm 1 (see also Fig. 4).

4 Numerical tests

All simulations presented in this section have been implemented in the framework of the LGPL parallel finite element library LifeV (`http://www.lifev.org`). The LifeV code for the electromechanical coupling is currently available under request. Simulations were run on 1-16 nodes of the cluster Bellatrix at the EPF Lausanne (each with 2 Sandy Bridge processors running at 2.2 GHz, with 8 cores each, 32 GB of RAM, Infiniband QDR 2:1 connectivity, and GPFS filesystem). For reference, model parameters are described in Table 2 at page 18. Tetrahedral meshes were generated with the mesh manipulator GMSH (`http://www.geuz.org/gmsh`).

Algorithm 2 – Weak electromechanical coupling.

Set timestep τ_e, τ_m, initial and final time $t = t_0$ and t_F;
while $t < t_F$ **do**
  repeat
    Find $\boldsymbol{w}^{n+\tau_e}$, solving gating variables explicitly

$$\mathrm{d}_t \boldsymbol{w} - \boldsymbol{r}(V, \boldsymbol{w}) = \mathbf{0};$$

    Find $V^{n+\tau_e}$ by solving the monodomain equation (22) using an implicit-explicit scheme
    Find $\gamma_f^{n+\tau_e}$, solving activation model explicitly

$$\bar{\eta}_A \dot{\gamma}_f = F_A + \sum_{n=1}^{3} (-1)^n (n+1)(n+2) I_{4,f} \gamma_f^n.$$

    Update time: $t \leftarrow t + \tau_e$, $n \leftarrow n + \tau_e$
  until $t = \tau_m$
  Find $\mathbf{F}^{n+1}$, solving the static nonlinear mechanical problem deriving from (12) and (15) by Newton iterations (see also [30])

$$\nabla \cdot [\mathbf{P}(\gamma_f)] = \mathbf{0}.$$

end while

4.1 Discretization and algorithmic details

Piecewise continuous linear finite elements were employed for the approximation of all electromechanical fields. An operator-splitting method is used to solve separately reaction and diffusion parts of (22). Time integration of the reaction step is performed with a locally varying third-order Rosenbrock method (see e.g. [34]) with implicit treatment of linear terms, whereas the diffusion step is advanced in time with an implicit Euler scheme. The resulting linear systems are solved using a conjugate gradient method preconditioned by a four-level algebraic multigrid method. Insulation boundary conditions are applied to the electric potential, ionic variables and activation field. Initial data will be taken as in Table 2. The electromechanical system is solved using the assumption of weakly coupling between electrophysiology and mechanics. Different temporal resolutions are employed for each sub-problem: we subiterate the electrophysiology and the activation part, several times between every mechanical update. In particular, setting τ_e and τ_m the time step used for the electrophysiological problem and the timestep for the mechanical problem, respectively, we follow Algorithm 2. Near incompressibility of the tissue is enforced through the standard additive decomposition of the strain energy density into a volumetric and isochoric part [31]. The bulk modulus K for cardiac tissue is set to 350 kPa. To validate our numerical schemes and computational solver we performed a convergence test with respect to spatial discretization using $2^k \times 2^k \times 2^k$ elements meshes with $k = 1, \ldots, 5$. The main errors arise from the electrophysiology which requires a very fine mesh. An efficient strategy can be set up using different spatial resolutions for the electrical and mechanical systems. However, in the present work we use the same spatial resolution for both physical processes. The results shown for the first two test cases and for the third ventricular test were carried out using tetrahedral meshes of 3072 and 28416 elements, respectively. In the fourth test case, the mesh for the human ventricles consists of 2 millions elements.

4.2 Active strain evolution algorithm

From the computational point of view, when solving (18) special care is required in the evaluation of the consistency term $2I_{4,f}|_{n=n_0}$. This entails to record the initial configuration where the chemical quantity n is still at the resting value. To avoid this issue, and for sake of efficiency, we use a Taylor expansion of the term $\dfrac{\partial \psi_C}{\partial \mathbf{F}_A}$. In fact, denoting with

$$\mathcal{F}(\mathbf{u}, \gamma_f) = 2I_{4,f} / \left(1 + \gamma_f\right)^3,$$

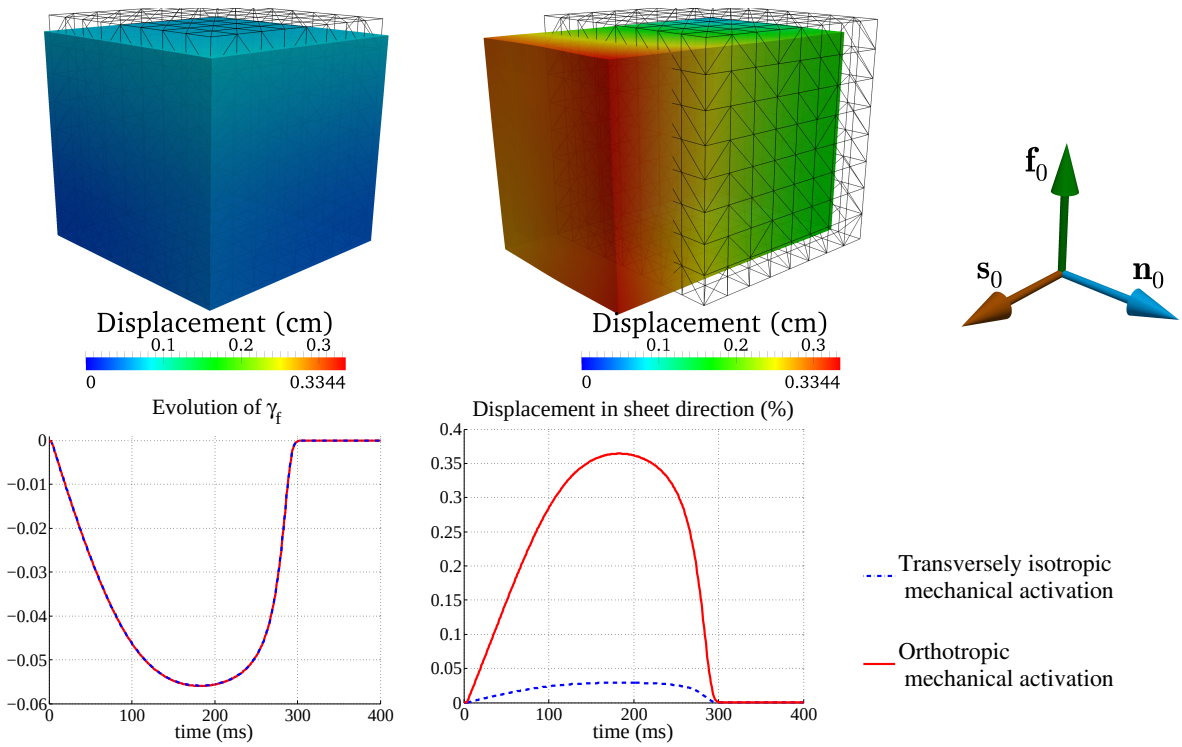

Figure 5: Test 1: Transversely isotropic (top left) and orthotropic (top center) activation. The evolution of γ_f (bottom left) is similar for both types of activations, but the displacement in the sheetlet direction (bottom center) is very small in the transversely isotropic case.

we perform a Taylor series expansion around $\gamma_f = 0$ as

$$\begin{aligned} \mathcal{F}(\mathbf{u}, \gamma_f) &= \sum_{j=0}^{\infty} \frac{\mathcal{F}^{(j)}(\mathbf{u}, 0)}{j!} \gamma_f^j \\ &= \sum_{j=0}^{\infty} (-1)^j (j+1)(j+2) I_{4,f} \gamma_f^j. \end{aligned} \tag{26}$$

Simple computations show that the series (26) has radius of convergence equal to 1 and therefore we can use it to approximate $\mathcal{F}(\mathbf{u}, \gamma_f)$ since we expect $\gamma_f \in [-0.15, 0]$. Noting also that $\mathcal{F}(\mathbf{u}, 0) = 2I_{4,f}|_{n=n_0}$ allows us to write an approximated version of (18) in the form

$$\bar{\eta}_A \dot{\gamma}_f = F_A + \sum_{j=1}^{M} (-1)^j (j+1)(j+2) I_{4,f} \gamma_f^j,$$

where we truncated the series at the $M-$th term and kept the same notation for the approximated variables, for simplicity. The linear case, for which $M = 1$, is not appropriate to represent (18) for values of γ_f smaller than -0.01. In the range $[-0.15, 0]$ the optimal value for M is found to be 5. For the reasons presented above, in the following numerical tests we will use the modified evolution law

$$\bar{\eta}_A \dot{\gamma}_f = F_A + \sum_{j=1}^{5} (-1)^j (j+1)(j+2) I_{4,f} \gamma_f^j, \tag{27}$$

which allows computational savings and easier calculations.

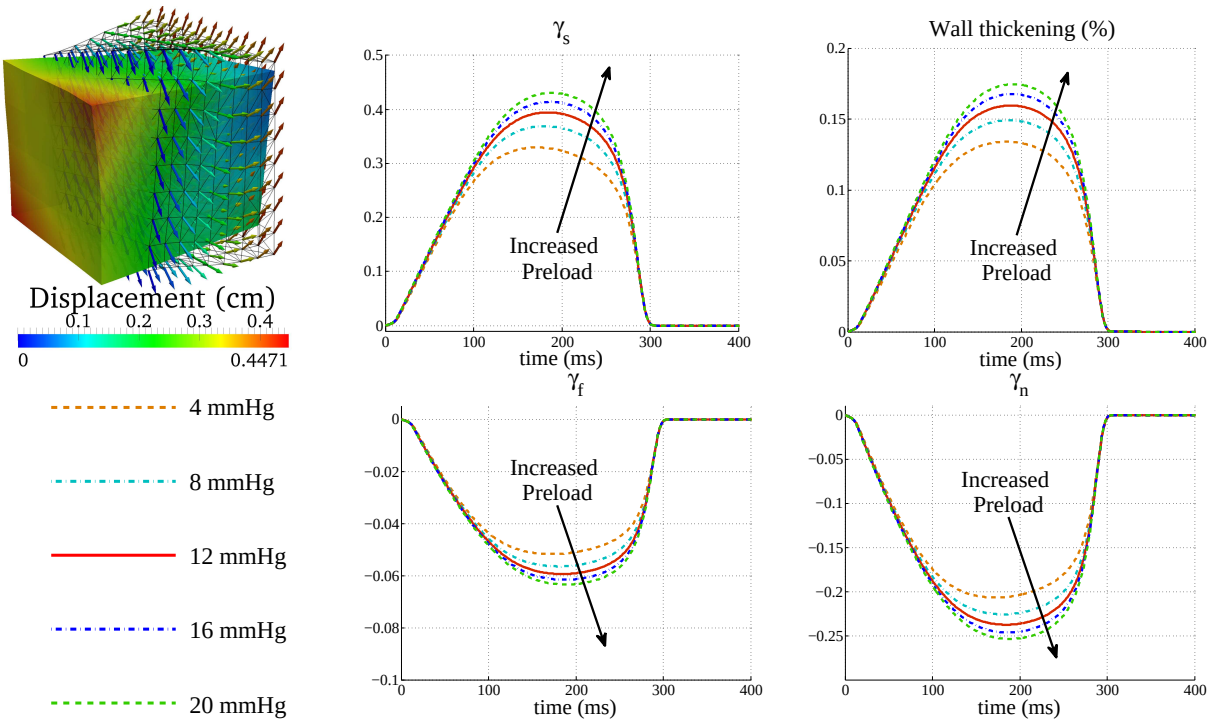

Figure 6: Test 2: The transmural cube is preloaded with an endocardial diastolic pressure which elongates the fibers. The direct introduction of the force-length relationship (19) in (27) leads to an increase wall thickening when the preload is increased. Top left: initial configuration (grid), fiber field(arrows) for 16 mmHg of preload and wall thickening at maximum contraction. The displacement magnitude is computed with respect to the preloaded configuration. Top center and top right: macroscopic active strain in sheetlet direction γ_s and wall thickening for different values of initial preload. Bottom center and bottom right: macroscopic fiber and cross-fiber strains γ_f and γ_n for different values of initial preload.

4.3 Test 1: Quasi compatible deformations

In this first test case we examine the differences between the typical transversely isotropic (see e.g. [11, 45, 14]) and the orthotropic mechanical activation proposed herein. As computational domain we consider the cube $\Omega_0 = [0,1] \times [0,1] \times [0,1]$ where the excitation front is initiated on one face, that is, $V(t_0) = \chi_{[0,0.05]\times[0,1]\times[0,1]}$. The fiber field is aligned in the $Y-$axis direction while the sheetlet field is aligned with the $X-$axis. Since the propagation of the depolarization front deriving from (22) is much faster than the increase of mechanical activation, the variable γ_f will be almost constant in Ω_0. Therefore, using proper boundary conditions for the mechanical problem the system will assume a stress-free compatible configuration. Namely, stress-free and symmetry boundary condition are imposed as follows: $\mathbf{P}\boldsymbol{\nu} = 0$ on Γ_N and $\mathbf{u}\cdot\boldsymbol{\nu} = 0$ on Γ_D, where $\Gamma_D = \{0\}\times[0,1]\times[0,1] \cup [0,1]\times\{0\}\times[0,1] \cup [0,1]\times[0,1]\times\{0\}$ and $\Gamma_N = \partial\Omega_0 - \Gamma_D$. In Fig. 5 (top row) we show the deformed configuration at maximum contraction for the transversely isotropic case, with $\gamma_n = \gamma_s$ (left) and for the orthotropic case $\gamma_n = \kappa\gamma_f$ (center), where we used the orthotropy parameter $\kappa = 4$. Fibers and sheetlets directions are shown in the frame of reference $\{\boldsymbol{f}_0, \boldsymbol{s}_0, \boldsymbol{n}_0\}$ at the top right. For both cases the average value of γ_f in Ω_0 and the maximum displacement in the sheetlet direction are displayed in Fig. 5 (bottom row). For both transversely isotropic and orthotropic mechanical activation, the minimum value of macroscopic (and microscopic) shortening in the fiber direction γ_f reached is about -0.06, in agreement with experimental data found in [36]. On the other hand the transversely isotropic case clearly fails to capture the very large strains in the sheetlet direction, with 3% of thickening against the 37% for the orthotropic case.

The small amount of thickening in the cross-fiber direction suggests that the transversely isotropic microscopical shortening is not sufficient to explain the large deformations taking place at the organ

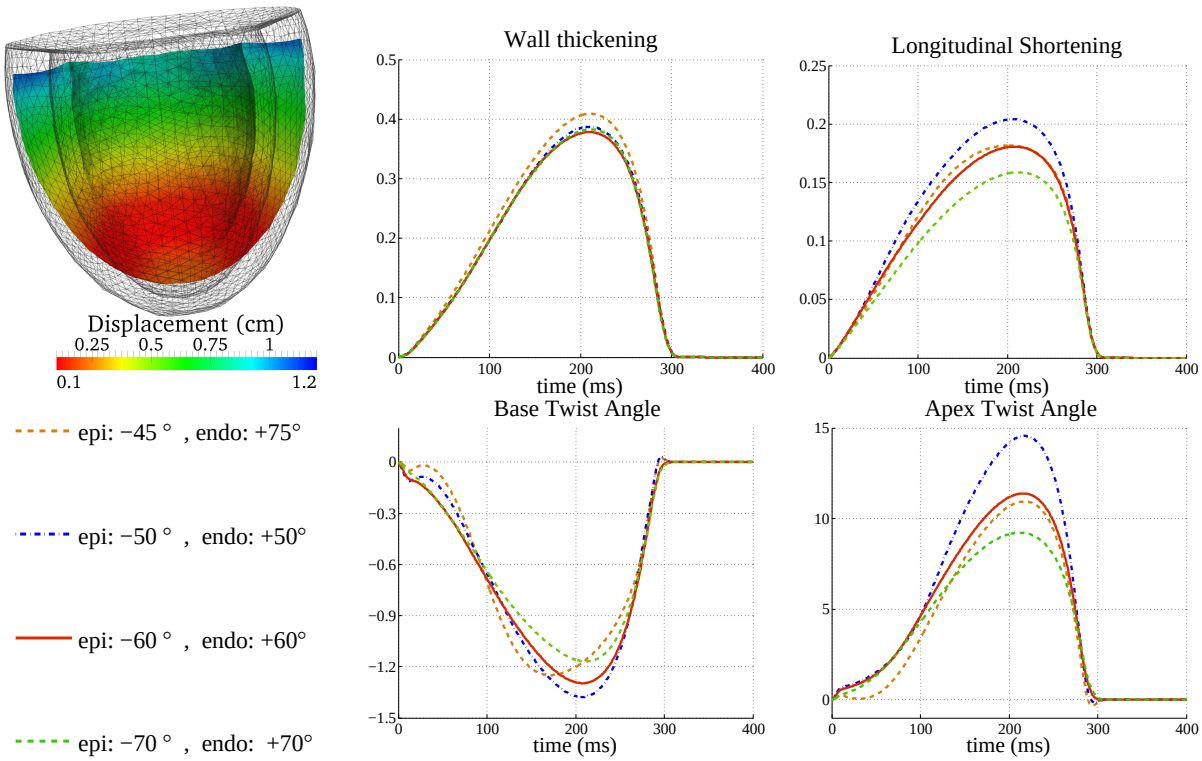

Figure 7: Test 3: The idealized ventricle is preloaded with 15 mmHg. Afterwards the depolarization wave is initiated on the full endocardium. To avoid excessive constraints on the motion, the ventricle is not fixed anywhere, which leads to a substantial longitudinal (apex-to-base) shortening. The amount of longitudinal shortening, as well as the twist angle at the base and at the apex of the ventricle strongly depend on the fiber orientation, while the amount of wall thickening does not. Top left: preloaded (grid) and systolic configurations. Top center: amount of wall thickening measured at 2 cm below the base for different fiber angles. Top right: longitudinal (apex-to-base) shortening for different fiber angles. Bottom center: Epicardial twist angle at a point at the base for different fiber angles. Bottom right: Epicardial twist angle at a point at the apex for different fiber angles.

level. This result is sufficient to drop the transversely isotropic hypothesis and consider a more general orthotropic mechanical activation hypothesis (8) that is able to capture deformations also at macroscopic level.

4.4 Test 2: Transmural slab

In the second test case we examine the role of diastolic preload and of the force-length relationship (19) introduced in (27). Once again we consider the slab $\Omega_0 = [0,1] \times [0,1] \times [0,1]$, representative of a small piece of transmural tissue, and we initiate the depolarization wave on the endocardial surface $\Gamma_{endo} = \{0\} \times [0,1] \times [0,1]$, i.e., $V(t_0) = \chi_{[0,0.05]\times[0,1]\times[0,1]}$. By $\Gamma_{epi} = \{1\} \times [0,1] \times [0,1]$ we denote the epicardial surface. We assume that the sheetlet direction is orthogonal to both Γ_{endo} and Γ_{epi}, and therefore parallel to the $X-$axis: $\boldsymbol{s}_0 = [1, 0, 0]^T$. A fiber rotation angle between Γ_{endo} and Γ_{epi} in the $X-$axis is considered and described by the relation $\theta = \pi/3 - (2\pi/3)X$. We define, in this way, $\boldsymbol{f}_0 = [0, \sin\theta, \cos\theta]^T$. Boundary conditions have been set as follows: pressure condition on the endocardial surface, that is $\mathbf{P}\boldsymbol{\nu} = p\boldsymbol{\nu}$, where p is the preload pressure, on Γ_{endo}; fixed point condition in the center of the epicardial surface, to prevent rigid translations, that is $\mathbf{u} = \mathbf{0}$ for $(X, Y, Z) = (1, 0.5, 0.5)$; fixed epicardial normal displacement, $\mathbf{u} \cdot \mathbf{n} = \mathbf{0}$ on Γ_{epi}; stress free conditions ($\mathbf{P}\boldsymbol{\nu} = 0$) are enforced elsewhere.

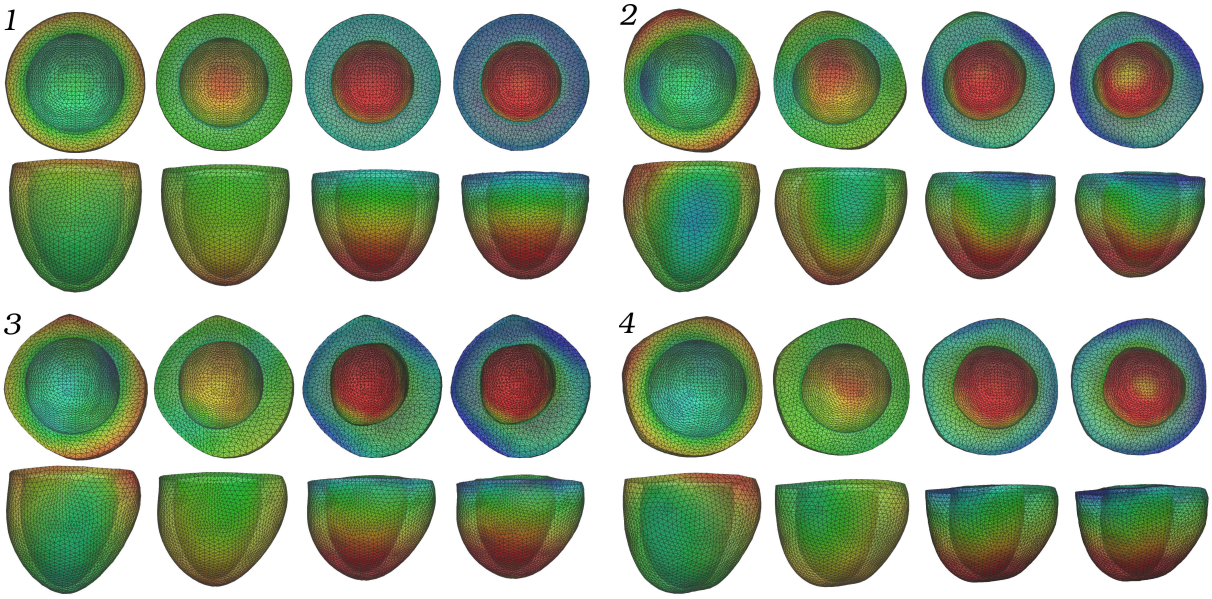

Figure 8: Test 3: Snapshots of the systolic phase on the idealized ventricle (1) and with non-symmetric ventricular geometries (2,3,4). The epi-endocardial fiber angle is set to be -60° + 60°. Break of geometrical symmetry leads to higher rotation angles. Refer to Fig. 7 for the colorbar. First rows: wall thickening; second rows: longitudinal shortening.

Diastolic preload was chosen (according to the values reported in [11, 18]) to range between 4 mmHg and 20 mmHg. In particular we took 5 steps of 4 mmHg as shown in Fig. 6 (bottom left). The higher the preload the greater the wall thickening, thanks to the action of the force-length relationship. Fig. 6 shows that this increase is not linear. When the preload is 20 mmHg, then the initial fiber elongation reached the optimal value in the force-length relationship. Therefore we expect a reduced contractility for a preload higher than 20 mmHg. Note, on the other hand, that the nonlinearity of the passive structural constitutive law (9) and the high stiffness in the fiber direction prevent excessive stretching.

In Fig. 6 we show the evolution of the average value of the macroscopic variables of γ_f, γ_s and γ_n and the wall thickening, defined as the mean distance between the endocardial and the epicardial surfaces Γ_{endo} and Γ_{epi}. To achieve a wall thickening of more than 30% the value of the orthotropic parameter was set to $\kappa = 4$. The model parameters for the evolution of γ_f are set to: active viscosity coefficient $\hat{\eta} = 5000\,\mathrm{s}\,\mu\mathrm{M}^{-2}$; active force parameter $\alpha = 4\,\mu\mathrm{M}^{-2}$, normalized diastolic chemical species $n_0 = 0.2155\,\mu\mathrm{M}$.

4.5 Test 3: Left ventricle contraction

Several indicators have been measured to characterize the left ventricular function. Our model assumptions are focused in capturing wall thickening. To validate our model, on the other hand, we now consider other indicators: the apex-to-base longitudinal shortening, the basal twist angle and the apical twist angle. Usually, when one of those indicators is not well captured, the poor knowledge of the fiber field or the lack of data about collagen sheetlet direction are blamed. For this reason, on the top of an idealized ventricular geometry represented by a truncated ellipsoid, we constructed four fiber fields using Algorithm 1. We aim in this way at a better understanding of the role of the fiber direction. The first fiber field used the values indicated in [8], with non-symmetric endocardial and epicardial angles ($\theta_{epi} = -45°$, $\theta_{endo} = +75°$). The other three fields have been constructed starting from the classical values ($\theta_{epi} = -60°$, $\theta_{endo} = +60°$) with 10° of difference, namely ($\theta_{epi} = -50°$, $\theta_{endo} = +50°$) and ($\theta_{epi} = -70°$, $\theta_{endo} = +70°$). The idealized ventricle is geometrically described as a truncated ellipsoid. The longitudinal endocardial radius is 6.4 cm long whereas the minor axis is 2.8 cm long. The thickness

of the wall in the reference configuration is set to 1.5 cm at the base and 0.6 cm at the apex. The depolarization wave is initiated on the full endocardium. On the epicardium and on the basal cut, we enforced Robin boundary conditions, $\mathbf{P} \cdot n = k\mathbf{u}$, with $k = 3.75$ mmHg cm^{-1}. On the endocardial surface we impose an initial preload of 15 mmHg. Pressure is increased during contraction but no pressure-volume relation is imposed.

In Fig. 7 we show the evolution of the aforementioned indicators. The ventricular configuration is shown at the top left, over the initial state (grid). From this analysis we see that the influence of the fiber direction on wall thickening (top center) is small, as the enlargement in all cases is between 37-41%. Longitudinal shortening (top right) instead, is influenced by the fiber angle. In fact, since the greater shortenings take place in the cross-fiber direction, then, smaller (in absolute value) angles will give rise to increased longitudinal shortening. Epicardial twist angles measured at the base and at the apex (bottom center and bottom apex) are strongly depending on the fiber direction. In fact, the peak rotation angle varies up to 50% in the considered cases. Results shown in Fig. 7 are in general agreement with experimental results [23, 37]. Even if basal twist angle is underestimated, which may be due to the high Robin coefficient imposed in the boundary conditions, we note that the twist and counter-twist behavior [21] are captured.

Apart from fiber orientation, geometrical aspects may also play a significant role, especially regarding twist angles. We used random free-form deformations to modify the idealized ventricular geometry and obtained three non-idealized left ventricles. On the deformed ventricles is difficult to find a good and consistent quantitative measure of twist angles. A qualitative way to note the increased twist is the break of symmetry of the displacement field of the idealized ventricle (Fig. 8(1-2-3-4)). To outline the geometrical effects, in all geometries, we used a fiber field such that $(\theta_{epi} = -60°, \theta_{endo} = +60°)$. In Fig. 8 we show snapshots of the systolic phase. On the top lines we notice the large wall thickening (40%), while in the bottom line we appreciate longitudinal shortening. The longitudinal shortening in all cases was in the range 18.5 ± 1.5 %. A series of videos of these simulations is available at CMCS official website (`http://cmcs.epfl.ch/applications/heart`).

4.6 Test 4: Human heart

As a final test case, we consider the human heart, where our objective is to show that the proposed model is consistent also in more realistic settings. Starting from a biventricular geometry segmented from CT scan data and a tetrahedral mesh consisting of 450k vertices and 2M elements [40], we employed Algorithm (1) to construct a rule-based sheet and fiber field. The initial electrical stimulus has been applied in the apical region of the right ventricle endocardium and in a central region of the left ventricle endocardium. All the model parameters and boundary conditions have been set as in the previous test case. We show in Fig. 9 the result of the full electromechanical coupling on the human heart: the generated fiber field on the left; the initial preloaded configuration, with 15 mmHg for the left ventricle and 8 mmHg for the right ventricle, in the center; the predicted systolic configuration on the right. The model worked "out of the box" in this test recovering roughly 40% of wall thickening and 20% of longitudinal shortening. Even if a fine tuning of the parameters as well as precise information about the fiber and sheet fields would be necessary to represent patient-specific cardiac cycles, this biventricular test case prove the potential of the model proposed herein. A video of the full simulation is available as online supplementary material.

5 Discussion

Experiments on isolated cardiomyocytes indicate that the cells contract mainly along their longitudinal axis. Assuming volume conservation of individual cells, this means that cells undergoing uni-axial contraction must expand in the two orthogonal directions. This has been used to justify active contraction models of cardiomyocytes, where the contribution from the active stress/strain acts mainly in the mean fiber direction in a transversely isotropic way. The orthotropic structure of the myocardium, dictated by the local fiber and sheetlet directions, is usually only accounted for in the passive material response.

Table 2: Typical values for model parameters.

Ionic cell model parameters
$u_0 = 0$, $u_u = 1.58$, $\theta_v = 0.3$, $\theta_w = 0.015$, $\theta_v^- = 0.015$, $\theta_o = 0.006$, $\tau_{v1}^- = 60$, $\tau_{v2}^- = 1150$, $\tau_v^+ = 1.4506$, $\tau_{w1}^- = 70$, $\tau_{w2}^- = 20$, $k_w^- = 65$, $u_w^- = 0.03$, $\tau_w^+ = 280$, $\tau_{fi} = 0.11$, $\tau_{o1} = 6$, $\tau_{o2} = 6$, $\tau_{so1} = 43$, $\tau_{so2} = 0.2$, $k_{so} = 2$, $u_{so} = 0.65$, $\tau_{s1} = 2.7342$, $\tau_{s2} = 3$, $k_s = 3.0994$, $\tau_{si} = 2.8723$, $\tau_{w\infty} = 0.07$, $w_\infty^* = 0.94$
Monodomain model parameters
$C_m = 1\mu\text{F/cm}^2$, $\chi = 1400\,\text{cm}^{-1}$, $\sigma_f = 1.3341\,\text{k}\Omega^{-1}\text{cm}^{-1}$, $\sigma_s = 0.176\,\text{k}\Omega^{-1}\text{cm}^{-1}$
Electrophysiology initial data
$w_0 = V = 0$, $w_1 = 1.0$, $w_2 = 1.0$, $w_3 = 0.02155$
Force-length relationship parameters
$c_0 = -4333.618335582119$, $c_1 = 2570.395355352195$, $c_2 = 1329.53611689133$, $c_3 = 104.943770305116$, $d_1 = -2051.827278991976$, $d_2 = 302.216784558222$, $d_3 = 218.375174229422$, $l_0 = 1.95\,\mu\text{m}$, $\text{S}L_{min} = 1.7\,\mu\text{m}$, $\text{S}L_{max} = 2.6\,\mu\text{m}$
Active strain parameters
$\alpha = -4\ \mu\text{M}^{-2}$, $\hat{\mu}_A = 5000\ \text{s}\ \mu\text{M}^{-2}$, $n_0 = 0.2155\ \mu\text{M}$, $\kappa = 4$
Passive material law parameters
$a = 0.333\,\text{kPa}$, $a_f = 18.535\,\text{kPa}$, $a_s = 2.564\,\text{kPa}$, $a_{fs} = 0.417$, $K = 350\,\text{kPa}$, $b = 9.242$, $b_f = 15.972$, $b_s = 10.446$, $b_{fs} = 11.602$

However, there is no reason to assume that the correct strategy for upscaling is to assume that the behavior at the macroscopic level of cardiac tissue is directly inherited from the microscopic level of individual cells. The microstructure of the myocardium is complicated and is comprised not only of fibers and fiber sheetlets, but also of the fibrous extracellular collagen matrix making a formal homogenization difficult. The structure of the sheetlets may influence the macroscopic behavior just as much as the fiber orientation, and this fact is not captured by a transversely isotropic contraction model. Many models found in the literature consider active stress/strain only in the fiber directions, and, as a result, produce simulations with rather unrealistic contraction patterns with reduced wall thickening during diastole and little to no apex-to-base shortening (or in some cases even lengthening, resulting in squeezed and elongated ventricle shapes). The inaccurate prescription of fiber and sheetlet directions is sometimes given as the reason for this, and it is postulated that if only more accurate structural information about fiber sheetlets in the myocardium was available, the results would be more in line with what is observed in *in vivo* hearts. Instead, we argue that it is important to modify the active constitutive law of the mechanical activation to take into account the macro-structurally induced transversal anisotropy.

Following Ståhlhand *et al.* [44, 45, 46] we have performed a thermodynamically consistent derivation of the active mechanics of contracting cardiac tissue that is valid for both active strain and active stress based models. We have shown that, in the latter case, it is possible to derive simple phenomenological laws, similar to the commonly used model of Nash and Panfilov [28], by introducing an additional internal state variable which links the biochemical reactions to the macroscopic stress. In the active strain formulation, the internal state variable linking the macroscopic and the microscopic is represented by the "active" part of the deformation gradient tensor. To bridge the gap between force generation at the microscopic level and tissue contraction at the macroscopic level we have presented a phenomenological model for transversely anisotropic active strain -driven contraction through a decomposition of the total active deformation gradient into a microscopic deformation gradient and a macroscopic deformation gradient.

Following this idea, we propose a simple geometrical mechanism that can explain the observed cross-fiber shortening. Our main assumption is that the cardiomyocytes are surrounded by an inextensible

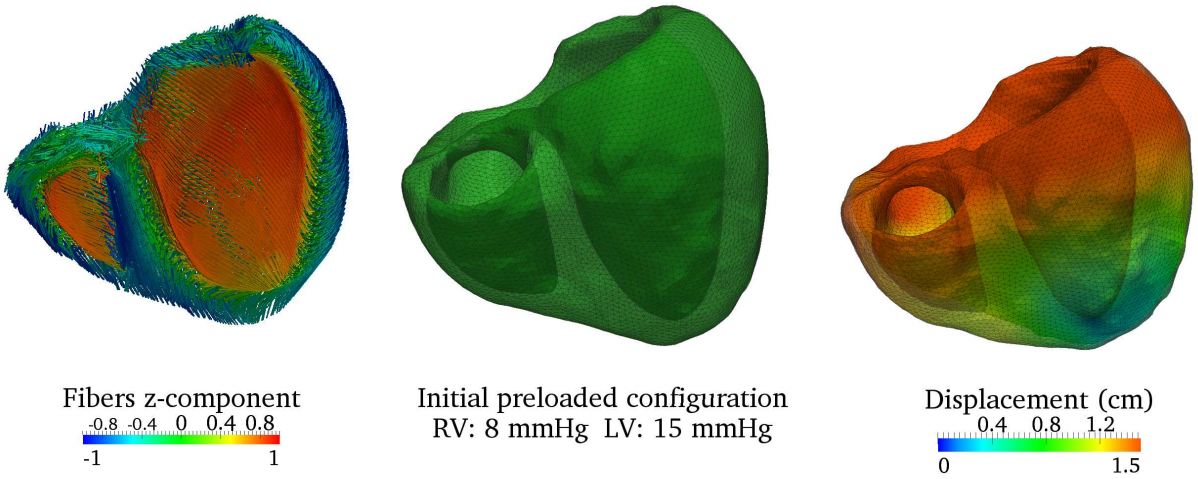

Figure 9: Test 4: a rule-based fiber field has been created (left) for a human ventricular geometry [40]. The left and right ventricles have been preloaded (center) with a pressure of 8 mmHg and 15 mmHg, respectively. Systolic configuration of the human ventricles (right).

framework of collagen fibers that constrains their macroscopic deformation in the cross-fiber direction, similarly to the hypothesis made in [4]. Wall thickening is then achieved by imposing volume conservation at the macroscopic level. This simple geometrical model leads, after linearization, to assume that the macroscopic deformation in the cross-fiber direction is proportional to the microscopic deformation in the fiber direction. This fact is also confirmed by experimentally observed strain measurements and capture the effect due to the fiber sheetlets sliding against each other leading to about 40% of wall thickening. In this work the proportionality constant is fixed – its correct value is the subject of additional study both from an experimental and a theoretical point-of-view. In reality, the cross-fiber strains are roughly three/four times larger than the strains in the fiber direction when measured at the endocardium, but diminish as one moves through the transmural thickness to the epicardium [36]. Our model is tested using simulations on a simple cube, on idealized left ventricular ellipsoids as well as on more realistic human biventricular geometries with fiber and sheetlet orientations. In the resulting simulations three important phenomena are captured: the wall thickening up to 40% during peak-systole, the axis-to-base shortening of around 15%, and the ventricular torsion ranging from $-1°$ at the base to $+8°$ at the apex. Due to the explicit introduction of a force-length relationship inside the active force term along the fiber direction, the model also well reproduces the Frank-Starling effect as the preload inside the ventricle is increased.

A limitation of our model is that we have applied a phenomenological model linking the intracellular calcium to the active force generation, whereas it is standard to use a crossbridge kinetics model that more accurately predicts the prolonged force generated by the binding of myosin crossbridges with the actin sites. Most of the models we use are phenomenological in nature but can be calibrated to match typical values in the human species. For some models no human data is available, such as the force-length relationship, which is adapted from experiments with felines. We do not consider the effect of stretch-activated channels, nor perform a precise calibration of the ventricular pressure to match a desired pressure-volume curve. Including these aspects would make the simulations more physiological, but even with such a phenomenological framework we have shown that realistic contraction patterns of the ventricle can be obtained with relatively simple models once the constitutive law of the mechanical activation model is properly chosen to account for the macroscopic anisotropy.

Acknowledgments

We acknowledge the financial support by the European Research Council through the Advanced Grant *MATHCARD, Mathematical Modelling and Simulation of the Cardiovascular System*, Project 227058 and FCT through the Project EXCL/MAT-NAN/0114/2012. We also acknowledge Centro de Matemática e Aplicações (CEMAT) and the FCT grant SFRH/ BD/ 51067/ 2010. Finally, the authors wish to thank Federico Negri for the support with FFD, Simone Pezzuto and Paolo Tricerri for their contribution in software development, Olivier Rousseau for the initial human biventricular geometry and fiber orientation data, and Aymen Laadhari for his contribution in mesh postprocessing.

References

[1] Ambrosi, D., Pezzuto, S., 2011. Active stress vs. active strain in mechanobiology: constitutive issues. J. Elast. 107(2):199–212.

[2] Bogaert, J., Rademakers, F.E., 2001. Regional nonuniformity of normal adult human left ventricle. Am. J. Physiol. Heart. Circ. Physiol. 280(2):H610–H620.

[3] Böl, M., Abilez, O.J., Assar, A.N., Zarins, C.K., Kuhl, E., 2012. In vitro / in silico characterization of active and passive stresses in cardiac muscle. Int. J. Multiscale Comp. Engrg. 10:171–188.

[4] Bourdarias, C., Gerbi, S., Ohayon, J., 2009. A pseudo active kinematic constraint for a biological living soft tissue: An effect of the collagen network. Math. Comput. Model. 49(11–12):2170–2181.

[5] Bueno-Orovio, A., Cherry, E.M., Fenton, F.H., 2008. Minimal model for human ventricular action potentials in tissue. J. Theor. Biol. 253(3):554–560.

[6] Cherubini, C., Filippi, S., Nardinocchi, P., Teresi, L., 2008. An electromechanical model of cardiac tissue: Constitutive issues and electrophysiological effects. Prog. Biophys. Mol. Biol. 97(2–3):562–573.

[7] Coleman, B.D., Noll, W., 1963. The thermodynamics of elastic materials with heat conduction and viscosity. J. Chem. Phys. 13:167–178.

[8] Colli Franzone, P., Pavarino, L.F., Scacchi, S., Taccardi, B., 2008. Modeling ventricular repolarization: Effects of transmural and apex-to-base heterogeneities in action potential durations. Math. Biosci. 214(1–2):140–152.

[9] Dal, H., Göktepe, S., Kaliske, M., Kuhl, E., 2013. A fully implicit finite element method for bidomain models of cardiac electromechanics. Comp. Meth. Appl. Mech. Engrg. 253:323–336.

[10] Dubrovin, B.A., Fomenko, A.T., Novikov, S.P., 1992. Modern Geometry–methods and Applications: The geometry of surfaces, transformation groups, and fields (2nd ed.), Springer.

[11] Eriksson, T.S.E., Prassl, A.J., Plank, G., Holzapfel, G.A., 2013. Influence of myocardial fiber/sheet orientations on left ventricular mechanical contraction. Math. Mech. Solids 18(6):592–606, 2013.

[12] Epstein, M., 2012. The Elements of Continuum Biomechanics. John Wiley & Sons, Chichester.

[13] Göktepe, S., Acharya, S.N.S., Wong, J., Kuhl, E., 2011. Computational modeling of passive myocardium. Int. J. Num. Meth. Biomed. Engrg. 27:1–12.

[14] Göktepe, S., Kuhl, E., 2010. Electromechanics of the heart: a unified approach to the strongly coupled excitation–contraction problem. Comput. Mech. 45:227-243.

[15] Göktepe, S., Menzel, A., Kuhl, E., 2013. Micro-structurally based kinematic approaches to electromechanics of the heart. In: Holzapfel, G.A., Kuhl, E. (eds.), Computer Models in Biomechanics: From Nano to Macro, Springer-Verlag, pp. 175–187.

[16] Holzapfel, G.A., Ogden, R.W., 2009. Constitutive modelling of passive myocardium: a structurally based framework for material characterization. Phil. Trans. R. Soc. Lond. A 367:3445–3475.

[17] Hunter, P.J., Nash, M.P., Sands, G.B., 1997. Computational Electromechanics of the Heart, Computational Biology of the Heart. John Wiley and Sons, London, pp. 346–407.

[18] Klingensmith, M.E., Chen, L.E., Glasgow, S.C., 2008. The Washington manual of surgery. Wolters Kluwer Health/Lippincott Williams & Wilkins, Philadelphia.

[19] Lee, E.H., Liu, D.T., 1967. Finite strain elastic-plastic theory with application to plane-wave analysis. J. Appl. Phys. 38:17–27.

[20] LeGrice, I.J., Takayama, Y., Covell, J.W.J., 1995. Transverse shear along myocardial cleavage planes provides a mechanism for normal systolic wall thickening. Circ. Res. 77:182–193.

[21] Lorenz, C. H., Pastorek, J. S., Bundy, J.M., 2000. Delineation of normal human left ventricular twist throughout systole by tagged cine magnetic resonance imaging. J. Cardiov. Magn. Reson. 2:2, 97–108.

[22] MacGowan, G.A., Shapiro, E.P., Azhari, H., Siu, C.O., Hees, P.S., Hutchins, G.M., Weiss, J.L., Rademakers, F.E., 1997. Noninvasive measurement of shortening in the fiber and cross-fiber directions in the normal human left ventricle and in idiopathic dilated cardiomyopathy. Circulation 96:535–541.

[23] MaxIver, D.G., 2012. The relative impact of circumferential and longitudinal shortening on left ventricular ejection fraction and stroke volume. Exp. Clin. Cardiol. 17(1):5–11

[24] Menzel, A., Steinmann, P., 2007. On configurational forces in multiplicative elastoplasticity. Int. J. Solids Struct. 44(13):4442–4471.

[25] Murtada, S., Kroon, M., Holzapfel, G.A., 2010. A calcium-driven mechanochemical model for prediction of force generation in smooth muscle. Biomech. Model. Mechanobiol. 9:749–762.

[26] Nagler, A., Bertoglio, C., Gee, M., Wall, W., 2013. Personalization of cardiac fiber orientations from image data using the unscented Kalman filter. In: Ourselin, S., Rueckert, D., Smith, N. (eds.), Functional Imaging and Modeling of the Heart, Lecture Notes in Computer Science, Vol. 7945, Springer-Verlag, Berlin-Heidelberg, pp. 132–140.

[27] Nardinocchi, P., Teresi L., 2007. On the active response of soft living tissues. J. Elast. 88:27–39.

[28] Nash, M.P., Panfilov, A.V., 2004. Electromechanical model of excitable tissue to study reentrant cardiac arrhythmias. Prog. Biophys. Mol. Biol. 85:501–522.

[29] Negroni, J.A., Lascano, E.C., 2008. A simulation of steady state and transient cardiac muscle response experiments with a Huxley-based contraction model. J. Mol. Cell Cardiol. 45(2):300–12.

[30] Nobile, F., Quarteroni, A., Ruiz-Baier, R., 2012. An active strain electromechanical model for cardiac tissue. Int. J. Numer. Meth. Biomed. Engrg. 28:52–71.

[31] Ogden, R.W., 1984. Non-Linear Elastic Deformations, Dover Publications Inc.

[32] Pathmanathan, P., Chapman, S.J., Gavaghan, D., Whiteley, J.P., 2010. Cardiac electromechanics: the effect of contraction model on the mathematical problem and accuracy of the numerical scheme. Quart. J. Mech. Appl. Math. 63:375–399.

[33] Pustoc'h, A., Ohayon, J., Usson, Y., Kamgoue, A., Tracqui, P., 2005. An integrative model of the self-sustained oscillating contractions of cardiac myocytes. Acta Biotheor. 53(4):277–293.

[34] Quarteroni, A., Sacco, R., Saleri, F., 2007. Numerical Mathematics, Series: Texts in Applied Mathematics, Vol. 37. 2nd ed. Springer-Verlag, Milan.

[35] Quinn, T.A., Kohl, P., 2013. Combining wet and dry research: experience with model development for cardiac mechano-electric structure-function studies. Cardiovasc. Res. 97(4):601–611.

[36] Rademakers, F.E., Rogers, W.J., Guier, W.H., Hutchins, G.M., Siu, C.O., Weisfeldt, M.L., Weiss, J.L., Shapiro, E.P., 1994. Relation of regional cross-fiber shortening to wall thickening in the intact heart. Three-dimensional strain analysis by NMR tagging. Circulation 89:1174-82.

[37] Reyhan, M., Li, M., Gupta, H., Llyod, S.G., Dell'Italia, L.J., Kim, H.J., Denney, T.S., Ennis, D., 2013. Left ventricular twist and shear-angle in patients with mitral regurgitation. J. Cardiov. Magn. Reson. 15:P92.

[38] Rice, J.J., Wang, F., Bers, D.M., de Tombe, P.P., 2008. Approximate model of cooperative activation and crossbridge cycling in cardiac muscle using ordinary differential equations. Biophys. J. 95:2368–2390.

[39] Rossi, S., Ruiz-Baier, R., Pavarino, L.F., Quarteroni, A., 2012. Orthotropic active strain models for the numerical simulation of cardiac biomechanics. Int. J. Numer. Meth. Biomed. Engrg. 28:761–788.

[40] Rousseau, O., 2010. Geometrical modeling of the heart. PhD thesis, Université d'Ottawa.

[41] Ruiz-Baier, R., Ambrosi, D., Pezzuto, S., Rossi, S., Quarteroni, A., 2013. Activation models for the numerical simulation of cardiac electromechanical interactions. In: Holzapfel, G.A., Kuhl, E. (eds.), Computer Models in Biomechanics: From Nano to Macro, Springer-Verlag, pp. 189–201.

[42] Ruiz-Baier, R., Gizzi, A., Rossi, S., Cherubini, C., Laadhari, A., Filippi, S., Quarteroni, A., 2013. Mathematical modeling of active contraction in isolated cardiomyocytes. Math. Medicine Biol., DOI:10.1093/imammb/dqt009.

[43] Sharifimajd, B., Stålhand, J., 2013. A Continuum model for skeletal muscle contraction at homogeneous finite deformations. Biomech. Model. Mechanobiol., DOI:10.1007/s10237-012-0456-x.

[44] Stålhand, J., Klarbring, A., Holzapfel, G.A., 2008. Smooth muscle contraction: Mechanochemical formulation for homogeneous finite strains. Prog. Biophys. Mol. Biol. 96:465–481.

[45] Stålhand, J., Klarbring, A., Holzapfel, G.A., 2011. A mechanochemical 3D continuum model for smooth muscle contraction under finite strains. J. Theoret. Biol. 268:120–130.

[46] Stålhand, J., Klarbring, A., Holzapfel, G.A., 2013. Modeling of smooth muscle activation. In: Holzapfel, G.A., Kuhl, E. (eds.), Computer Models in Biomechanics: From Nano to Macro, Springer-Verlag, pp. 77–92.

[47] Strobeck J.E., Sonnenblick E.H., 1986. Myocardial contractile properties and ventricular performance. In: Fozzard, H.A., Haber, E., Jennings, R.B., Katz, A.M., Morgan, H.E. (eds.), The heart and cardiovascular system, Raven, New York, pp. 31–49.

[48] Taber, L.A., Perucchio, R., 2000. Modeling heart development. J Elast. 61(1-3):165–197.

[49] Tracqui, P., Ohayon, J., Boudou, T., 2008. Theoretical analysis of the adaptive contractile behaviour of a single cardiomyocyte cultured on elastic substrates with varying stiffness. J. Theor. Biol. 255(1):92–105.

[50] Yaniv, Y., Sivan, R., Landesberg, A., 2006. Stability controllability and observability of the four state model: Model of the sarcomere control of contraction. Annals Biomed. Engrg. 34:778–789.

[51] Washio, T., Okada, J., Sugiura, S., Hisada, T., 2012. Approximation for cooperative interactions of a spatially-detailed cardiac sarcomere model. Cell. Mol. Bioeng. 5:113–126.

[52] Wong, J., Kuhl, E., 2013. Generating fiber orientation maps in human heart models using Poisson interpolation. Comp. Meth. Biomech. Biomed. Eng., DOI:10.1080/10255842.2012.739167.

[53] Xia, H., Wong, K., Zhao, X., 2012. A fully coupled model for electromechanics of the heart. Comput. Math. Methods. Med., 2012:927279.

Recent publications :

MATHEMATICS INSTITUTE OF COMPUTATIONAL SCIENCE AND ENGINEERING
Section of Mathematics
Ecole Polytechnique Fédérale
CH-1015 Lausanne

15.2013 D. KRESSNER, J. E. ROMAN:
Memory-efficient Arnoldi algorithms for linearizations of matrix polynomials in Chebyshev basis

16.2013 D. KRESSNER, M. MILOLOZA PANDUR, M. SHAO:
An indefinite variant of LOBPCG for definite matrix pencils

17.2013 A. ABDULLE, M. J. GROTE, C. STOHRER:
FE heterogeneous multiscale method for long time wave propagation

18.2013 A. ABDULLE, Y. BAI, G. VILMART:
An online-offline homogenization strategy to solve quasilinear two-scale problems at the cost of one-scale problems

19.2013 C.M. COLCIAGO, S. DEPARIS, A. QUARTERONI:
Comparison between reduced order models and full 3D models for fluid-structure interaction problems in haemodynamics

20.2013 D. KRESSNER, M. STEINLECHNER, B. VANDEREYCKEN:
Low-rank tensor completion by Riemannian optimization

21.2013 M. KAROW, D. KRESSNER, E. MENGI:
Nonlinear eigenvalue problems with specified eigenvalues

22.2013 T. LASSILA, A. MANZONI, A. QUARTERONI, G. ROZZA:
Model order reduction in fluid dynamics: challenges and perspectives

23.2013 M. DISCACCIATI, P. GERVASIO, A. QUARTERONI:
The interface control domain decomposition (ICDD) method for the Stokes problem

24.2013 V. LEVER, G. PORTA, L. TAMELLINI, M. RIVA:
Characterization of basin-scale systems under mechanical and geochemical compaction

25.2013 D. DEVAUD, A. MANZONI, G. ROZZA:
A combination between the reduced basis method and the ANOVA expansion: on the computation of sensitivity indices

26.2013 M. SHAO:
On the finite section method for computing exponentials of doubly-infinite skew-Hermitian matrices

27.2013 A. ABDULLE, G. VILMART, K. C. ZYGALAKIS:
High order numerical approximation of the invariant measure of ergodic SDEs

28.2013 S. ROSSI, T. LASSILA, R. RUIZ-BAIER, A. SEQUEIRA, A. QUARTERONI:
Thermodynamically consistent orthotropic activation model capturing ventricular systolic wall thickening in cardiac electromechanics